Available online at www.sciencedirect.com
ScienceDirect
Journal of Magnetic Resonance 185 (2007) 1–11
JMR Journal of Magnetic Resonance
www.elsevier.com/locate/jmr

A unilateral NMR magnet for sub-structure analysis in the built environment: The Surface GARField

P.J. McDonald [a,*], P.S. Aptaker [b], J. Mitchell [a], M. Mulheron [c]

[a] School of Electronics and Physical Sciences, University of Surrey, Guildford, Surrey GU2 7XH, UK
[b] Laplacian Ltd., D5 Culham Science Centre, Culham Innovation Centre, Abingdon, Oxon OX12 9LY, UK
[c] School of Engineering, University of Surrey, Guildford, Surrey GU2 7XH, UK

Received 31 August 2006; revised 31 October 2006
Available online 22 November 2006

Abstract

A new, portable NMR magnet with a tailored magnetic field profile and a complementary radio frequency sensor have been designed and constructed for the purpose of probing *in situ* the sub-surface porosity of cement based materials in the built environment. The magnet is a one sided device akin to a large NMR-MOUSE with the additional design specification of planes of constant field strength $|\mathbf{B}_0|$ parallel to the surface. There is a strong gradient G in the field strength perpendicular to these planes. As with earlier GARField magnets, the ratio $G/|\mathbf{B}_0|$ is a system constant although the method of achieving this condition is substantially different. The new magnet as constructed is able to detect signals 50 mm (^{1}H NMR at 3.2 MHz) away from the surface of the magnet and can profile the surface layers of large samples to a depth of 35–40 mm by moving the magnet, and hence the resonant plane of the polarising field, relative to the sample surface. The matching radio frequency excitation/detector coil has been designed to complement the static magnetic field such that the polarising $\mathbf{B}_0$ and sensing $\mathbf{B}_1$ fields are, in principal, everywhere orthogonal. Preliminary spatially resolved measurements are presented of cement based materials, including two-dimensional T_1–T_2 relaxation correlation spectra.

Keywords: Unilateral NMR; Portable MRI; GARField; Two-dimensional relaxation correlations

1. Introduction

In the field of materials characterisation there is a considerable and growing interest in the ability to probe nuclear magnetic resonance (NMR) parameters from an embedded region of a sample that is itself too large, or immobile, to fit within the confines of a traditional NMR magnet. These are studies to which one-sided or open-access magnets with tailored inhomogeneous magnetic fields are particularly suited. Two primary classes of device that have led the way in development of *in situ* NMR are oil well-logging tools [1–3] and hand-held mobile universal surface explorer (NMR-MOUSE®)[1] [4] sensors. Oil well-logging has driven considerable technological development and advancement of inhomogeneous field NMR theory and practice. NMR logging tools are now widely used in the field and come in several variants. The basic NMR-MOUSE is able to probe a few millimetres into a sample surface. As such it has found niche applications as diverse as the study of water damage to ancient frescoes [5] and the *in situ* characterisation of car tyres [6]. Again there are several variants with different relative advantages and disadvantages.

An application area that is beginning to come to the fore is the study of cement based building materials. On the one hand, this includes the analysis of fresh cement paste hydration and the subsequent development of porosity [7–10]. On the other, it extends to studies of the long-term degradation of cement due to, for example, the transport and build-up of sub-surface water [11,12]. For hydration

* Corresponding author. Fax: +44 1 1483 686781.
E-mail address: P.Mcdonald@surrey.ac.uk (P.J. McDonald).
[1] NMR-MOUSE is a registered trade mark of RWTH-Aachen, Germany.

1090-7807/$ - see front matter © 2007 Published by Elsevier Inc.
doi:10.1016/j.jmr.2006.11.001

and degradation studies, sub-surface depths up to about 50 mm are of interest for several reasons: (a) this is the typical maximum depth of protective and decorative toppings; (b) this is the typical depth of concrete cover over reinforcement bars and; (c) this is the region of water activity that commonly leads to structural degradation in the long term. Several groups have proposed specific magnet designs that could be used for this application, for instance Fukushima and Jackson [13], Callaghan et al. [14], and Marble et al. [15]. As yet, however, none of these systems has proved totally ideal or gained widespread acceptance and preference over the others.

In this contribution, we further develop the design philosophy of a GARField (Gradient At Right angles to the Field) magnet [16,17]. We previously proposed GARField magnets with curved pole-pieces for the high spatial resolution profiling of thin samples with a layered structure, such as polymer films [18], glues [19], and human skin [20,21]. GARField magnets are characterised by a magnetic field which is of constant magnitude in a horizontal plane and which has a strong gradient in the field strength orthogonal to this plane. In the original GARField implementation, this plane is situated between the two specially shaped, curved pole pieces. The surface GARfield magnet developed here extends the concept to a one-sided design. The design draws directly from a linear eddy-current brake [22].

The new surface GARField magnet has been briefly introduced in a previous paper [23]. Here we discuss the magnet design and the specific advantages and distinct differences of this design compared to other magnets developed for similar applications. First, from the outset, we continue to target an inhomogeneous magnetic field that is of a constant magnitude in a finite flat plane. The area of the plane is of comparable size to the magnet and is parallel to the surface of both the magnet and structure under study. Consequently, it is straightforward to obtain depth resolved information. Second, we address the problem that the radio frequency (RF) excitation field should also be of constant magnitude parallel to the surface and should be everywhere orthogonal to the static field. This leads to the development of a complementary probe that is designed to specifically match the field plot of the magnet. We show profiles of rubber phantoms used to calibrate the system and some preliminary data from cement and concrete samples exposed to varying environmental conditions.

It is of course intended that many of the experiments currently performed on rock formations with well-logging tools or on lamellar structures with the NMR-MOUSE should be performed on cements and concretes with the new device. Consequently we show preliminary spatially resolved profiles of water (^{1}H NMR) distribution in large cementitious blocks. We also demonstrate two-dimensional T_1–T_2 relaxation correlation spectra [24] of water in cement obtained during hydration using the one-sided device. It is well documented that the nuclear spin relaxation times T_1 and T_2 are sensitive to variations in the surface-to-volume ratio of pores [25,26]. In these two-dimensional experiments, the T_1 relaxation is encoded during the first measurement period and the T_2 relaxation encoded during the second period when the data is recorded. A two-dimensional inverse Laplace transform provides the correlation of the first parameter T_1 with the second parameter T_2. The two-dimensional T_1–T_2 results presented for white cement in this work are compared to results from a homogeneous bench-top magnet published previously [27]. A particular advantage of the two-dimensional correlation experiment in cements is that the influence of paramagnetic impurities which otherwise leads to uncertainty in the data interpretation is significantly reduced since it is possible to infer the T_1/T_2 ratio.

2. Magnet development

In NMR, spins are sensitive to the modulus of both the polarising magnetic field $|\mathbf{B}_0|$ and the RF sensor field $|\mathbf{B}_1|$, and the relative angle between them. The original GARField design developed curved pole pieces to provide a series of planes of constant $|\mathbf{B}_0|$ with a strong fixed orthogonal gradient for spatial discrimination. The Surface GARField is designed to create the same end result from a single-sided magnet. The ideal theoretical solution is a linear Halbach array [28]. Such a magnet can be approximated by a line of magnetic blocks oriented one to the next at a modest number of discrete angles. However, even simpler alternatives still provide a good field profile at the sample distance. The practical implementation developed here ultimately derives from the permanent magnet primary of an electrical machine, e.g. a linear eddy-current brake [22]. In a linear eddy-current brake the magnet array (primary) is attached to an object sliding along a conducting rail (secondary). The eddy-currents induced in the rail by the magnet array provide a braking force approximately proportional to the velocity of the object.

Magnet design can be approached in terms of magnetisation or current densities. Since we are developing both a magnet and a matched RF coil, we can use either: we choose the current density formalism. Consider a current sheet infinite in the x–z plane. The sheet is in air and current only flows in the x-direction. The current density is made periodic in the z-direction with a period $\lambda = 2\pi/\alpha$. The current density, $K_x(z)$, can be expressed as a Fourier series, *viz*.:

$$K_x(z) = \sum_{m=0}^{\infty} K_{x,m} \sin(m\alpha z). \tag{1}$$

From symmetry, the magnetic field, $\mathbf{B}$, above and below the sheet is in the y–z plane. The B_x component is everywhere zero. Hence the magnetic field has the form:

$$\mathbf{B}(z,y) = B_z(z,y)\mathbf{k} + B_y(z,y)\mathbf{j}, \tag{2}$$

where $\mathbf{i}$, $\mathbf{j}$, $\mathbf{k}$ are the unit vectors of the Cartesian coordinates x, y, z.

The z-component of the field immediately above ($\mathbf{B}^+$) and below ($\mathbf{B}^-$) the sheet is determined using Ampere's law:

$$\mathbf{j}\times\left(\frac{\mathbf{B}^+}{\mu_0}-\frac{\mathbf{B}^-}{\mu_0}\right)=K_x\mathbf{i}. \tag{3}$$

This leads to a B_z component on the upper surface given by:

$$B_z(z,0^+)=\tfrac{1}{2}\mu_0 K_x(z). \tag{4}$$

The factor of 1/2 is present because the current sheet is in air. If the sheet is placed on a steel plate, an image current forms thereby doubling the field strength and removing this factor. Applying $\nabla\cdot\mathbf{B}=0$ everywhere and the boundary conditions $\mathbf{B}\to 0$ as $y\to\infty$ leads to:

$$B_z(z,y)=\sum_{m=1}^{\infty}\mu_0 K_{x,m}\sin(m\alpha z)\mathrm{e}^{-m\alpha y} \tag{5}$$

and

$$B_y(z,y)=\sum_{m=1}^{\infty}\mu_0 K_{x,m}\cos(m\alpha z)\mathrm{e}^{-m\alpha y}. \tag{6}$$

The equivalence between the current sheet and a block of magnetised material of thickness d, uniform in the x-direction and magnetised in the y-direction with components of magnetisation M_y, is given by

$$\mathbf{K}=\mathbf{i}\left(-d\frac{\partial M_y}{\partial z}\right). \tag{7}$$

If the material is additionally magnetised in the z-direction then the sum of two equal current sheets is required, one above and one below the material. This gives an equivalent current density on the top and the bottom surfaces defined by $\mathbf{j}\times(\mathbf{M}^+-\mathbf{M}^-)=\mathbf{K}$, where $\mathbf{M}^+$ and $\mathbf{M}^-$ are, respectively, the magnetisation just above and just below the sheet, so $K_x(y=0)=+M_z$ and $K_x(y=-d)=-M_z$.

A linear Halbach array is one possible implementation in which the magnetisation vector continuously rotates along the z-axis. The ideal Halbach array is infinite in the x–z plane. The magnetic field above the array contains only one Fourier harmonic with a maximum magnetisation of M_1^{Halbach} and is given by:

$$\mathbf{B}=(\mu_0\alpha d)\mathrm{e}^{-\alpha y}M_1^{\mathrm{Halbach}}[\cos(\alpha z)\mathbf{j}+\sin(\alpha z)\mathbf{k}]. \tag{8}$$

This result guarantees a field of constant magnitude at a given height y above the array. In practice the magnetisation cannot be continuously rotated: it is not possible to achieve a field defined by a single Fourier component. Nor can the magnet extend indefinitely in the x–z plane: there will be end truncation effects on all sides of a finite magnet array. For practical implementations it is necessary to use a finite sequence of blocks that reduces the continuous rotation to a number of discrete steps. While large numbers of blocks per cycle offers a good approximation to the ideal, it is more convenient to consider scenarios with fewer blocks and in particular arrays in which the magnets are oriented only in or out of plane, such as 2 or 4 block cycles.

3. Magnet construction

We focus on the two-block sequence with blocks magnetised both uniformly and only in the y-direction, although much of the following detail can be readily applied to the more complex scenarios. Unfortunately this simplification leads to the creation of multiple Fourier harmonics so that the field intensity above the magnet has the components:

$$B_z(z,y)=\sum_{m=0}^{\infty}(\mu_0 m\alpha d)\mathrm{e}^{-m\alpha y}M_{y,m}\sin(m\alpha z) \tag{9}$$

$$B_y(z,y)=\sum_{m=0}^{\infty}(\mu_0 m\alpha d)\mathrm{e}^{-m\alpha y}M_{y,m}\cos(m\alpha z) \tag{10}$$

where $M_{y,m}$ are the Fourier components of $M_y(z)$ in which $M_y(z)$ has only three values: $+M_y$, 0, or $-M_y$. It is important to note that the constant magnitude condition required of the $\mathbf{B}_0$ field can only be met with a single harmonic and so modifications are made to ensure the final magnetic field contains only the fundamental ($m=1$). The magnets are separated by a small distance and with reference to Fig. 1 it is evident that this causes all the even harmonics to be zero. By fixing the angle θ (as defined in Fig. 1) to be $\theta=\pi/6$ the third harmonic also equals zero. Consequently, the first higher harmonic to contribute is the 5th ($m=5$). The factor $\exp(-m\alpha y)$ in Eqs. (9) and (10) ensures that the contribution of this and all higher odd harmonics is negligible at distances from the surface of the magnet large compared to a fraction of the period of the magnet array. Consequently the resulting field at a modest sample distance is almost pure fundamental with a field profile described by

$$\mathbf{B}=(\mu_0\alpha d)\mathrm{e}^{-\alpha y}M_{y,1}[\cos(\alpha z)\mathbf{j}+\sin(\alpha z)\mathbf{k}] \tag{11}$$

where $M_{y,1}=(2\sqrt{3}/\pi)M_y$ is the fundamental harmonic y-component of the magnetisation. Ultimately we will be

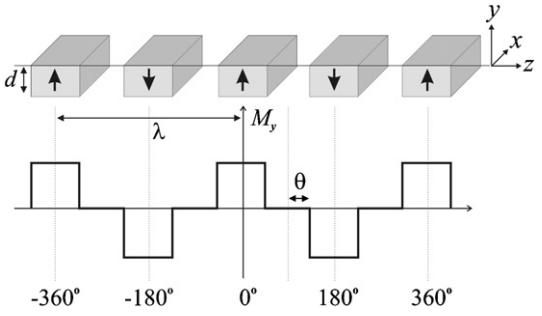

Fig. 1. Schematic showing the two block linear eddy-current array required to provide a field profile containing, to a good approximation, only a single Fourier harmonic. The block symmetry removes the even harmonics and angle θ is selected to remove the third. Other higher odd harmonics are negligible at distances large compared to λ from the magnet.

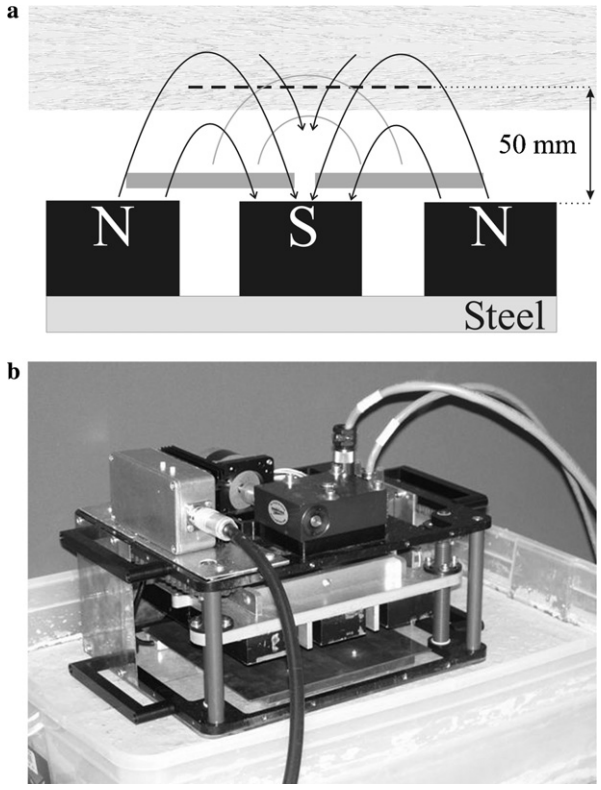

Fig. 2. (a) Schematic of the unilateral magnet. The three magnetic blocks produce the polarising field profile indicated by the black arrows. The sensor coil (grey bars) above the magnet provides an RF field (grey lines) that is everywhere orthogonal to the polarising field. Both fields have a near uniform modulus at a distance 50 mm above the surface of the magnet (dashed line). (b) The Surface GARField magnet as constructed, having been inverted and placed on a large concrete sample. The three magnetic blocks are visible mounted on the motorised platform. The whole assembly weighs less than 20 kg and can be lifted by a single person.

using thick magnetic blocks so this magnetisation will be less than the ideal maximum, M_1^{Halbach}. However, the inclusion of the steel backing plate effectively doubles the final magnetic field strength.

A similar argument can be used to design a surface sensor coil from current windings. The winding spacing can be varied across the coil so as to approximate a sinusoidal current distribution. If a periodic array of these coils is spatially offset from the magnetic block array by a distance equal to $\lambda/4$ then the condition that the two fields are everywhere orthogonal is automatically met.

The simplest possible magnetic block array has been constructed consisting of three neodymium iron boron (NdFeB) magnetic material elements; see Fig. 2(a). Analytic expressions for magnetic blocks were used to refine the magnet block positions so as to minimise truncation errors and thereby optimise the field. Vector Fields Opera 3D software[2] was subsequently used to verify and improve the optimisation. This was necessary since 3 blocks are, of course, an extreme approximation of an infinite array. Notwithstanding, it is possible to adjust the positions and width of the blocks to alleviate end truncation effects: the magnet mark space ratio is increased slightly, the central block is made slightly narrower, and the outer two blocks slightly wider than in the ideal infinite design. NdFeB magnets can suffer from large variations in coercivity H_c and remanence B_r which could impair performance of the fabricated device. The magnetic blocks used in the construction were all taken from the same batch and tested for outlier characteristics thereby limiting variation in B_r to $<2\%$ of the required uniform remanence. When in place the arrangement of magnets in the Surface GARField, with North and South poles adjacent, boosts the magnetisation and reduces the effects of low coercivity. The space between the magnetic blocks can provide other advantages. In particular it is possible to mount field modulation coils around the pole pieces.

The complementary RF coil is made from just two current winding elements on the same pitch as the magnets and placed symmetrically above them. Each winding consists of 10 turns spaced so as to reproduce the current distribution for a pure fundamental field, again slightly modified to alleviate truncation effects. The fact that the sensor is half a period short in the z-direction compared to the magnet and is also shorter in the x-direction means that the region over which $\mathbf{B}_1$ has significant constant magnitude in the plane falls off sooner than $\mathbf{B}_0$ thereby assisting lateral spatial selectivity.

The magnet as built has $\lambda = 150$ mm and a resonant frequency of 3.2 MHz in a plane 50 mm above its surface; see Fig. 2a. It is mounted on a motor drive enabling the magnet to be moved relative to the fixed sample surface and hence provide a profile without changing the resonant frequency. This is directly akin to the method of stray-field imaging (STRAFI), except that in conventional STRAFI measurements the sample is moved relative to a fixed magnet [29]. The actual Surface GARField can be seen in Fig. 2b.

4. Magnet validation

The numerically calculated magnetic field components for both the magnet and sensor on a line along the z-axis at $y = 50$ mm and $x = 0$ mm can be seen in Fig. 3. From these calculations it is possible to determine $G/|\mathbf{B}_0| = 38.46\ \text{m}^{-1}$. The three components for the $\mathbf{B}_0$ field, Fig. 3a, can clearly be seen to be zero in the x-direction, cosinusoidal in the y-direction, and sinusoidal in the z-direction as described by Eq. (11). Conversely the $\mathbf{B}_1$ field, Fig. 3b, exhibits a cosinusoidal variation in the z-direction. Hence the modulation of the y and z components of the $\mathbf{B}_0$ and $\mathbf{B}_1$ fields is $\pi/2$ out of phase. Significantly from these graphs it can be seen that the homogeneous region in the $|\mathbf{B}_1|$ field is much smaller than in the $|\mathbf{B}_0|$ field. The planar regions of the two fields coincide over an area of approximately $50 \times 50\ \text{mm}^2$. The total volume (depth) of the

[2] Vector Fields Ltd., 24 Bankside, Kidlington, Oxford OX5 1JE, UK.

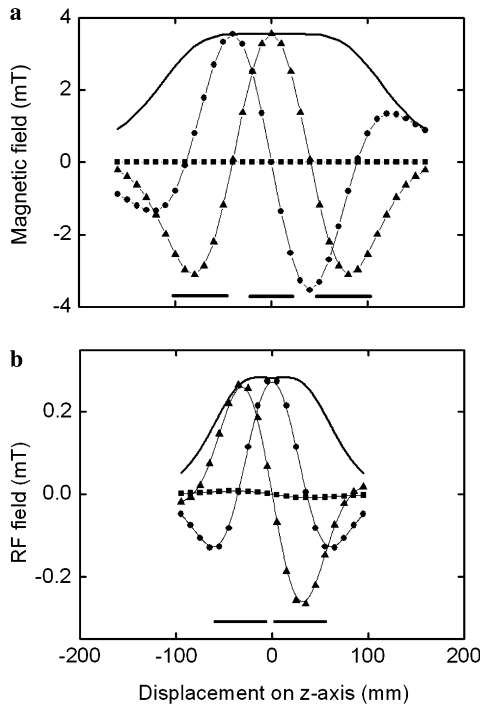

Fig. 3. Simulated field profile of (a) the $\mathbf{B}_0$ field components and, (b) the $\mathbf{B}_1$ field components when 1 A of current flows in the coil. These plots are located at $y = 50$ mm, $x = 0$ mm relative to the surface of the magnet. In each case the components are B_x (squares), B_y (triangles), B_z (circles), and $|\mathbf{B}|$ (solid line). The bars at the bottom of the graphs indicate the position and width of (a) the permanent magnetic blocks and (b) the RF sensor coils.

excitation slice is ultimately determined by the $\mathbf{B}_0$ field gradient and the RF pulse length.

The $\mathbf{B}_0$ field was measured in a plane 50 mm above the magnet surface using a Hirst VMG01 Virtual Gaussmeter with an accuracy of $\pm 1\%$, repositioned via a three axis stepper motor controller from Time Systems. A systematic error can be introduced if the Gaussmeter is not precisely aligned with the components of the field. The measured $|\mathbf{B}_0|$ field plot is shown in Fig. 4. This can be compared to the numerically calculated $|\mathbf{B}_0|$ field in the same plane shown in Fig. 3a. The two plots are similar, with only a slight deviation from the ideal field modulus in the polarising plane of the actual magnet. Due to truncation the lines of constant field in the z direction are slightly concave towards the magnet for small y, and slightly convex for larger y. The system was numerically optimised for a flat field profile at 50 mm assuming uniform magnetic remanence and coercivity in the blocks. Comparisons between the simulated and the measured field profiles suggest that the planar region of the polarising field actually occurs slightly further than 50 mm from the surface of the magnet.

5. Relaxation analysis

Protons (^{1}H) in the mobile water in cement based materials exhibit different relaxation time characteristics depen-

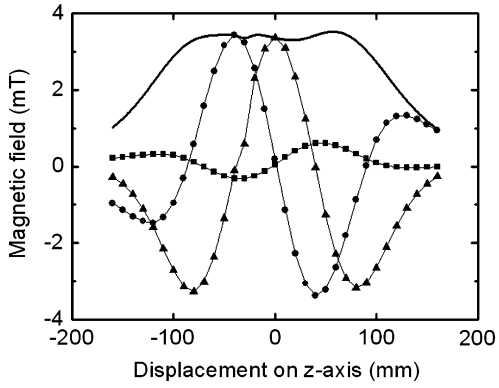

Fig. 4. The $\mathbf{B}_0$ field as measured at $y = 50$ mm, $x = 0$ mm above the surface of the constructed magnet. In each case the components are B_x (squares), B_y (triangles), B_z (circles), and $|\mathbf{B}_0|$ (solid line). The bars at the bottom of the graphs indicate the position and width of the permanent magnetic blocks.

dant on the degree of confinement and chemical interactions. When the surface-to-volume ratio (S/V) is very large, the surface contribution will dominate the observed relaxation time. In the case of rapid exchange between protons in the pore and on the pore surface, a single, average relaxation time is observed [25]

$$\frac{1}{T_{1,2}^{\text{observed}}} = \frac{1}{T_{1,2}^{\text{bulk}}} + \frac{\varepsilon S}{V}\frac{1}{T_{1,2}^{\text{surface}}}, \tag{12}$$

where T_1 and T_2 are the spin–lattice and spin–spin relaxation times, respectively, and ε is the thickness of the surface layer. It is usual for the first term to be small compared to the second so that the observed relaxation rate is directly proportional to S/V. If a distribution of pore sizes is present in the material, then there will be a corresponding distribution in the observed relaxation rates. This basic method has been demonstrated previously in cement based materials [7–10].

The surface relaxation rates of water molecules is determined by interactions with paramagnetic species S in the solid structure. According to a model proposed by Korb et al. [30,31], the temporarily adsorbed protons I undergo a two-dimensional walk across the pore surface and encounter the paramagnetic species S that cause variation in the local dipolar fields leading to an enhancement of the spin relaxation. By defining two correlation times, a surface hopping time τ_m and a surface residency time τ_s the model leads to an expression for the frequency dependent ratio of $T_2^{\text{surface}}/T_1^{\text{surface}}$ thus [27]:

$$\frac{T_2^{\text{surface}}}{T_1^{\text{surface}}} = 2\left\{\frac{3Ln\left(\frac{1+\omega_I^2\tau_m^2}{\left(\frac{\tau_m}{\tau_s}\right)^2+\omega_I^2\tau_m^2}\right) + 7Ln\left(\frac{1+\omega_S^2\tau_m^2}{\left(\frac{\tau_m}{\tau_s}\right)^2+\omega_S^2\tau_m^2}\right)}{4Ln\left(\left(\frac{\tau_s}{\tau_m}\right)^2\right) + 3Ln\left(\frac{1+\omega_I^2\tau_m^2}{\left(\frac{\tau_m}{\tau_s}\right)^2+\omega_I^2\tau_m^2}\right) + 13Ln\left(\frac{1+\omega_S^2\tau_m^2}{\left(\frac{\tau_m}{\tau_s}\right)^2+\omega_S^2\tau_m^2}\right)}\right\} \tag{13}$$

where ω_I is the proton resonant frequency and $\omega_S = 658.21\omega_I$ is the paramagnetic electron resonant frequency. From field cycling measurements on cements the

correlation time for the diffusion of temporarily adsorbed molecules on a pore surface τ_m has been estimated at 1.3 ns [32] leading to a pore surface residence time τ_s estimated at 18.5 μs. The results on white cement presented below were conducted on a 20 MHz Maran bench top spectrometer and the Surface GARField magnet at 3.2 MHz. From Eq. (2), these parameters correspond to a $T_1/T_2 = 4$ at 20 MHz and $T_1/T_2 = 2.25$ at 3.2 MHz.

6. Experimental

The Surface GARField NMR experiments were conducted using a Maran Ultra spectrometer[3] connected to a 2 kW low frequency RF power amplifier manufactured by Tomco Technologies.[4] To allow this amplifier to drive into the RF coil at 3.2 MHz, the complex frequency response of a conventional series-parallel tuned circuit has been replaced with a low Q series L-C-R circuit that has a purely real impedance of 12.5 Ω. This is matched to an impedance of 50 Ω using a 4:1 transformer. The resultant dead time is less than 100 μs.

To obtain orthogonality between the $\mathbf{B}_0$ and $\mathbf{B}_1$ fields the RF sensor must be mounted on the permanent magnet and both should be of the order of 50 mm from the region of interest. In practice, profiles have been recorded with the RF coil mounted in two different configurations. In the first configuration, the RF coil is mounted on the magnet and moved relative to the fixed sample surface as prescribed by the ideal case. This has the advantage that the same $|\mathbf{B}_1|$ field is present in all the sample volume-slices and so in principal no intensity corrections need be applied to the recorded signal as a function of depth. However, cement based materials can significantly alter the tuning of the RF circuit as a function of proximity, thereby causing a loss of signal that is difficult to calibrate. Whilst the probe could be re-tuned at different locations during the experiment, the signal amplitude obtained with this configuration is far less than the maximum possible signal intensity. The ability to probe cement samples with low proton densities is therefore severely limited using this configuration.

In the second configuration the maximum signal intensity is seen. The RF coil is mounted in a fixed position close to the sample surface. The polarising field moves relative to both the sample and RF field. Therefore the tuning of the RF detector circuit does not vary since the sensor is stationary. When using this configuration the power of the excitation pulses is altered during the acquisition of a profile to obtain the maximum signal possible at each point whilst maintaining a constant pulse length and hence sensitive slice thickness. This configuration immediately results in the orthogonality condition being less well met near the surface of the sample. Also the cement profiles have to be normalised using the signal from a uniform rubber phantom measured in the same way.

Profiles were obtained from rubber phantoms and cement blocks by measuring point-by-point in a step-wise fashion akin to STRAFI [29]. Each point in a profile is obtained either by integrating over 32 echoes from a quadrature echo β_x-[τ-β_y-τ-echo-]$_n$ sequence, or by fitting the echo train using an exponential decay function. The pulse length is $t_p = 18$ μs (corresponding to a slice ~0.37 mm thick, derived using a calculated field gradient of $G = 3.25\ \mathrm{Tm}^{-1}$ at the sensitive plane) and $\tau = 100$ μs. Thousand twenty four scans are recorded with a relaxation delay of 0.5 s. With these parameters the measurement of a profile of 30 points lasts less than 5 h.

The Surface GARField T_1–T_2 relaxation correlation experiments were performed on a $100 \times 100 \times 100\ \mathrm{mm}^3$ block of white cement. The same experiments as previously reported in a 20 MHz uniform field [19] were performed except that the pulse sequence was altered to utilise saturation, rather than inversion, recovery for the T_1 encoding. Also the quadrature echo sequence rather than CPMG was used for T_2 encoding. In this way all the pulse lengths could be made equal, ensuring that the signal always originated from a slice of approximately constant thickness within the inhomogeneous magnetic field. As at high field, the T_1 encoding times logarithmically spanned the range 0.1–1000 ms. However, due to the long dead-time inherent in the low-frequency system the quadrature echoes were linearly spaced every 0.2 ms rather than also being logarithmically distributed. Hence the total T_2 range spanned was less. The pulse length was $t_p = 11$ μs, corresponding to a slice thickness of ~0.6 mm some 10 mm below the surface of the sample. The RF pulse provided a nominal flip angle $\beta = 9°$ at the centre of the slice. With 128 averages, each complete measurement took 5 h.

7. Results

The profile obtained from three phantoms made from rubber moulding compound can be seen in Fig. 5. These profiles are all acquired using the first system configuration with both the probe and magnet moving relative to the sample. The spatial origin refers to the top of the magnet at the point of closest approach to the sample. The first 10 mm are occupied by the sensor coil. The phantoms were positioned on a 5 mm thick Perspex support from which no signal is detected.

The first profile shown, Fig. 5a (circles), is recorded into the surface of a uniform block of rubber with dimensions $100 \times 100 \times 100\ \mathrm{mm}^3$. The sensitive slice was slightly less than 0.4 mm thick, and was stepped through the sample in 1 mm increments, providing an overall pixel resolution of 1 mm. The signal-to-noise (S/N) ratio is constant over the whole profile as indicated by the error bars. The flat face of the block should ideally be a sharp step (2 pixels), but this has been spread over 2–3 mm by the curvature in $|\mathbf{B}_0|$ within the region of $|\mathbf{B}_1|$ sensitivity.

[3] Oxford Instruments Molecular Biotools Ltd., Tubney Woods, Abingdon, Oxon OX13 5QX, UK.

[4] Tomco Technologies, 17 Clarke Street, Norwood, SA 5067, Australia.

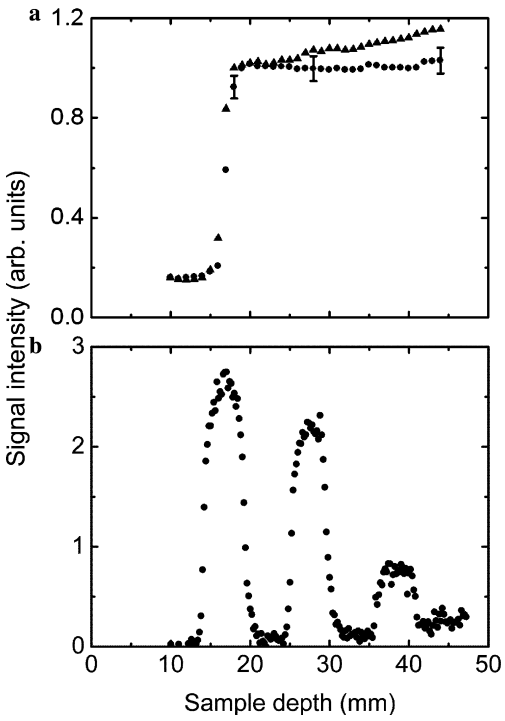

Fig. 5. (a) Profile of a uniform block of rubber with dimensions $100 \times 100 \times 100\ \text{mm}^3$ (circles), and from a larger rubber block with dimensions $300 \times 250 \times 100\ \text{mm}^3$ (triangles). (b) Profile of a phantom constructed from three sheets of rubber of constant thickness separated by Perspex spacers. The surface areas of the rubber sheets were $200 \times 200\ \text{mm}^2$, $100 \times 100\ \text{mm}^2$, and $50 \times 50\ \text{mm}^2$, left to right, respectively.

Beyond this step the block extends "infinitely" upward with little or no variation in proton density. As the sensitive plane of $|\mathbf{B}_0|$ sweeps through the sample, the profile height increases by up to 6% as additional signal is detected from the curved edges of the field. A larger block covering an area of $300 \times 250\ \text{mm}^2$, Fig. 5a (triangles), exhibits a larger 16% increase in signal across the profile since there are more protons being detected from the curved region of $|\mathbf{B}_0|$.

Fig. 5b shows a profile through a second phantom constructed from three sheets of rubber separated by Perspex spacers. Each sheet of rubber was 6 ± 0.5 mm thick. The polarising plane was stepped through the phantom in 0.2 mm intervals with both the magnet and sensor moving relative to the sample. In this profile the pulse length was increased to $t_p = 25\ \mu\text{s}$ so the sensitive slice thickness approximately equalled the step size. This provided a nominal pixel resolution of about 0.2 mm, although the overall resolution is closer to 2–3 mm. The surface area of the sheets varied in the order $200 \times 200\ \text{mm}^2$, $100 \times 100\ \text{mm}^2$, $50 \times 50\ \text{mm}^2$ (bottom to top), so that the total volumes of the rubber sheets were in the ratio 16:4:1. It is seen that the area under the profile peaks varies in the ratio 4:3:1 since the device is less sensitive to protons outside the planar region of $|\mathbf{B}_0|$. A slight increase in the baseline of the profile above the third sheet is a result of some signal being detected from a concrete weight placed on the top of the phantom.

It is clear from these results that the instrument in its current state of development is capable of providing a maximum pixel resolution of 0.2 mm over a depth of 45 mm under ideal conditions in the first configuration. We estimate that the critical plane of the Surface GARField surveys an area of slightly less than $100 \times 100\ \text{mm}^2$.

Fig. 6 shows a profile of the $100 \times 100 \times 100\ \text{mm}^3$ rubber phantom recorded using the second system configuration with the coil fixed near the sample surface. This profile has an overall pixel resolution of 1 mm. Maximum signal is obtained at the surface of the sample when the polarising plane is close to the sensor coil. The signal intensity was obtained by fitting single exponential decay curves to the multi-echo data on a point by point basis in order to permit calibration of cement profiles discussed below. Beyond the surface, the signal decreases almost exponentially as the sensitive plane moves away from the sensor. The loss in signal is due to the reduction in RF power available to excite the region of interest and reciprocal detector sensitivity. This is far more significant than any performance gain from the better meeting of the orthogonality condition as the polarising plane moves away from the sensor coil. Exemplar error bars have been added to indicate the corresponding decrease in S/N ratio as the signal reduces across the profile. Below we demonstrate the application of the Surface GARField to the study of porous building materials, such as cement and concrete.

It was not possible to record profiles from significant depths into cement blocks with significantly lower proton density and shorter effective T_2 using the first system configuration. Fig. 7 shows a profile through a $100 \times 100 \times 100\ \text{mm}^3$ white cement cube obtained using the second system configuration with the RF coil in a fixed position close to the surface. The profile intensity was obtained by exponential fitting on a point by point basis and normalised using the signal from the rubber phantom already shown in Fig. 6. The conversion of signal intensity to free water concentration in grams per gram was performed by cross

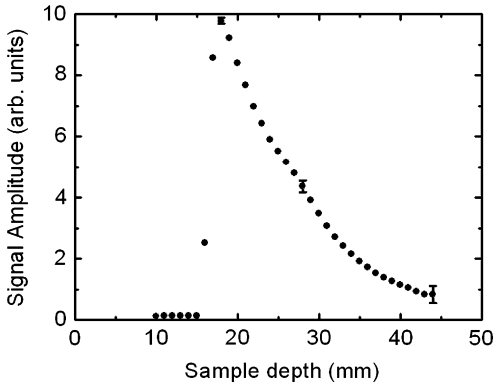

Fig. 6. Profile of a uniform block of rubber with dimensions $100 \times 100 \times 100\ \text{mm}^3$ measured with the sensor coil fixed close to the surface of the sample.

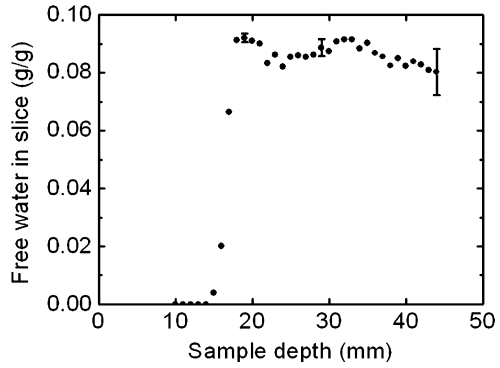

Fig. 7. Calibrated profile obtained from a three day old cube of white cement of dimensions $100 \times 100 \times 100$ mm^3. Error bars have been shown on exemplar points to indicate the change in signal-to-noise ratio across the profile. The front face of the cube is located between 16–17 mm depth.

reference to measurements of a pure water sample and rubber at 20 MHz in a uniform field. The calibration could not be performed directly at 3.2 MHz with the portable device due to the strong diffusive attenuation of the signal from the bulk water reference sample.

To demonstrate the use of the Surface GARField for examining existing structures, signal was obtained at various depths from a 1 month old 25 kg slab of concrete (cured and stored under water) as the top surface of the slab was allowed to dry in air: see Fig. 2b, using the second, fixed coil, system configuration. The concrete was mixed in the ratio 3:2:1:0.6 by mass of 10 mm aggregate, sand, cement, and water. A 5 kg section of concrete was cut away from the rest of the slab using a diamond wheel prior to drying and stored under identical conditions to allow a comparative gravimetric measurement to be recorded. In Fig. 8, signal was obtained near the sample surface (squares), and 10 mm (circles), 15 mm (triangles), and 20 mm (inverted triangles) below the surface over a period of 300 h. The data was obtained by fitting a single, average

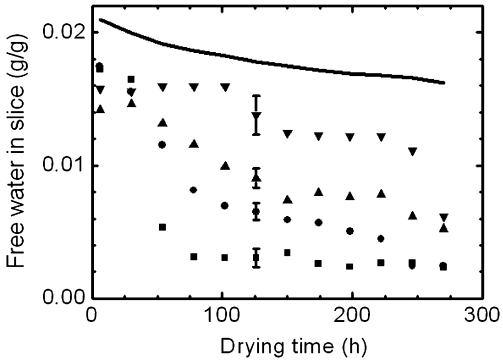

Fig. 8. Evaporable water content of a 20 kg concrete slab measured at upper surface (squares), 10 mm (circles), 15 mm (triangles), and 20 mm (inverted triangles) depth as the surface was allowed to dry in air. Gravimetric measurements, solid line, show the total variation in evaporable water mass over the same period.

exponential decay to the integrals of 32 individual echoes obtained using a quadrature echo train at each location. The signal was calibrated to a water fraction as previously described. In practice there was little difference between these profiles and those obtained simply by integrating over all the echoes. The single component fit overlooks the relaxation time weighting between the gel and capillary water. A slightly different result, but with greater error bars, was obtained with a two component exponential fit. The sensitivity of the measurement is reduced due to the volume of each slice occupied by aggregate: the signal intensity was estimated to be reduced to 22% of that from a hydrated cement sample with the same initial water to cement ratio. Initially the water content is the same at all depths, within the limits of experimental error. After 30 h of surface drying the signal from just below the sample surface reduced significantly as the water in the open pores evaporated. The water content between 10 and 15 mm below the sample surface reduced steadily after the first 30 h as the concrete dried, with the signal at 15 mm being consistently slightly higher than at 10 mm. The signal at 20 mm depth remained constant for the first 100 h before decreasing to approximately 75% of the initial value. The signal again remained constant for another 100 h before decreasing further. These results are as expected from a concrete slab with only the upper surface exposed to air. The water quickly evaporates from the surface porosity and then diffuses out of the lower layers over time. The gravimetric result (solid line, Fig. 8) is similar to the NMR results at depth. It shows a continuous decrease in the total evaporable water content over the 300 h experiment, at which point almost 25% of the evaporable water had been lost. The gravimetric result was calibrated by oven drying at the end of the experiment. Visual inspection of the sealed sides of the slab indicated the drying mainly occurring near the exposed upper surface of the concrete, where the NMR measurement was sensitive.

A potential application of the Surface GARField magnet is the *in situ* study of topping layers applied over concrete structures. The transport or accumulation of water at the interface between a surface coating or topping and the concrete base can lead to structural defects in the long term and is therefore of significance. To demonstrate the applicability of the Surface GARField magnet to this problem, a $100 \times 100 \times 100$ mm^3 concrete cube was cast with constituent components of 10 mm aggregate, sand, cement, and water in the ratio 3:2:1:0.6 by mass, respectively. This was allowed to cure for three days in a high humidity environment before a 10 mm thick topping of self-levelling floor compound was added, mixed in a water to powder ratio of 0.2 by mass. The sample was then wrapped in plastic film to prevent rapid drying. Profiles were recorded following the application of the topping; see Fig. 9a. This topping had hardened sufficiently to allow a profile to be recorded after 4 h (squares). Subsequent profiles were recorded after 24 (circles), 48 (triangles), and 72 h (inverted triangles). The profiles were constructed from integrated

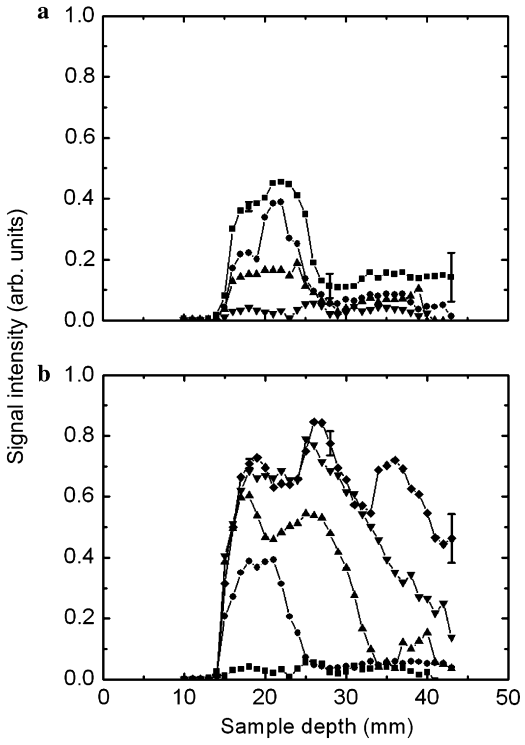

Fig. 9. (a) Profiles of a concrete cube (beyond 25 mm) with 10 mm of self levelling floor compound placed on top (15–25 mm). Profiles were recorded 41 h (squares), 24 h (circles), 48 h (triangles), and 72 h (inverted triangles) after topping was applied. (b) Profiles of same concrete/topping sample after water has been applied to the open topping surface for 0 h (squares), 24 h (circles), 48 h (triangles), 72 h (inverted triangles), and 96 h (diamonds). In both graphs the lines have been added as an aid to the eye.

echo intensities rather than point by point exponential fitting. This reduced the scatter in the data, particularly at low intensities, but prohibited the calibration in grams per gram of water due to different relaxation properties across the sample. Error bars have been added to indicate the change in sensitivity throughout the sample. These are larger in the concrete base due to the presence of the aggregate. A clear demarcation is visible between the topping (15–25 mm depth) and the concrete base (beyond 25 mm depth). This interface is broad due to a combination of the curvature in $|\mathbf{B}_0|$, the water distribution across the interface, and the uneven surface of the concrete base. As the topping continued to cure, more free water became chemically combined with cementitious material and the signal intensity decreased. The signal from the lower half of the topping increased over the first 24 h probably due to gravimetric draining of the free water. The signal from the concrete base is initially relatively high, indicating the presence of free water. After 24 h the signal from the concrete has reduced and remains at an almost constant value near the baseline noise for the next three days, although a further slight decrease over time may indicate ongoing cure. After 72 h virtually no signal was present in any region of the sample, suggesting an almost total absence of evaporable water.

Once the concrete block and topping had reached the stage where no evaporable water signal could be detected, the sample was inverted and the topping exposed to water by being placed on a wet sponge. The sample was removed from the sponge, re-sealed and profiled every 24 h, then placed back on the sponge. The recorded profiles are shown in Fig. 9b. After the first 24 h (circles), the topping had absorbed water although the base remained dry. The water then began to transfer across the interface into the concrete base. After 48 h (triangles) exposure, signal was observed up to ~10 mm into the concrete below the interface. An increase of signal can also be seen at the upper edge of the topping, likely due to an increased uptake of water. After 72 h (inverted triangles) the topping appeared to be saturated, although the signal still decreased with depth into the concrete base. The water content of the concrete reached a maximum after the topping had been exposed to water for 96 h (diamonds). This was confirmed by placing the entire sample under water for 24 h and re-profiling. This final profile (not shown) was almost identical to that observed after the topping had been exposed to water for 96 h. The uneven signal intensity throughout the water saturated concrete, when compared to the almost constant signal obtained initially in Fig. 9a, is suggestive of porosity that could not be re-filled by capillary imbibition, and spatially non-uniform curing and porosity due to the hydration conditions and draining. The use of this method can provide considerable information on the presence, state, and distribution of water over time in a real concrete structure.

A comparison of the T_1–T_2 two-dimensional relaxation correlation spectra from 5 day old white cement using a 20 MHz bench-top magnet and the 3.2 MHz unilateral Surface GARfield magnet can be seen in Fig. 10, top and bottom, respectively. The significance of the individual peaks in the data recorded using the 20 MHz magnet has previously been discussed in detail [27]. Four peaks are present parallel to the line $T_1 = T_2$ and are now thought to relate to (left to right) two sizes of CSH gel porosity (referred to as finer and coarser product) both created during hydration, and two sizes of partially filled capillary pores resulting from chemical shrinkage. These peaks can be seen to lie on the diagonal $T_1 = 4T_2$ as predicted by surface relaxation theory, see Eq. (13). The off-diagonal peak with $T_1 \gg T_2$ can be attributed to exchange of water molecules between the two CSH gel products [33].

It is immediately obvious that the relaxation data recorded using the 3.2 MHz Surface GARField (Fig. 10, bottom) is less detailed than that from the bench-top magnet. The S/N ratio is reduced due to the lower proton resonance frequency and sensitivity of the single-sided device. The span of the T_2 measurement is also more limited due to the pulse sequence. Notwithstanding it is possible to distinguish two peaks parallel to the $T_1 = T_2$ line. The lower, larger peak, is centred at $T_1 \sim 10^{-3}$ s and obviously relates to gel pores. The smaller peak at longer $T_1 \sim 6 \times 10^{-3}$ s could also relate to gel porosity, and it is therefore possible

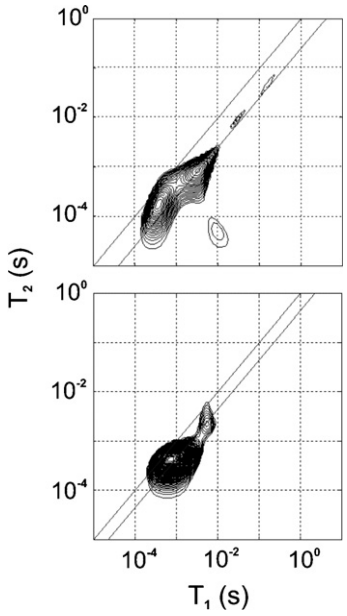

Fig. 10. T_1–T_2 two-dimensional relaxation correlation spectra for 5 day old white cement with a w/c ratio of 0.4 measured using a 20 MHz benchtop homogenous magnet (top) and the 3.2 MHz unilateral magnet (bottom). Both sets of graphs display prominent features distributed parallel to the $T_1 = T_2$ line.

that both the finer and coarser products are being observed. No capillary porosity is visible. However this is unsurprising due small quantity of water expected to be present in any partially filled capillary pores. Also in this sample no exchange peak is visible, perhaps due to the limitation on the minimum T_2 measurement. The peaks lie on the theoretically predicted line $T_1 = 2.25T_2$, the ratio of surface relaxation times being shifted due to the change in resonant frequency. From these results it suggests the magnet has the potential to non-destructively study the progress of hydration *in situ* within new structures at a level of detail that is not possible with other techniques.

8. Conclusion

A new addition to the GARField series of magnets has been demonstrated for the profiling of large samples up to depths of 35 mm. The design of this magnet has its origins mostly in the theory of a linear eddy-current array and uses a set of magnets with alternating polarity to provide a uniform plane of $|\mathbf{B}_0|$ some distance above the magnet surface. A sensor coil has also been developed using the same theory to provide a plane of uniform $|\mathbf{B}_1|$ where the components are everywhere orthogonal to those in $\mathbf{B}_0$. The magnet has so far been shown to be capable of providing high quality profiles of large samples. It can also be used to measure T_1–T_2 two-dimensional relaxation correlation plots in cement based materials—an extension to conventional relaxation methods that provides more information on the pore structure and degree of hydration in cement and concrete.

Acknowledgments

The authors thank The Royal Society for financial support, and Y.-Q. Song of Schlumberger-Doll Research for the use of the 2D Fast Laplace Inversion software.

References

[1] J.A. Jackson, R.K. Cooper, L.J. Burnett, J.F. Harmon, Remote NMR well logging, Geophysics 46 (1981) 415.
[2] M. Locatelli, An NMR logging apparatus with centimeter resolution, Revue De L Institut Francais Du Petrole 53 (1998) 477.
[3] R.L. Kleinberg, Well logging, in: D.M. Grant, R.K. Harris (Eds.), Encyclopedia of NMR, Wiley, New York, 1996, pp. 4960–4969.
[4] G. Eidmann, R. Savelsberg, P. Blümler, B. Blümich, The NMR MOUSE, a mobile universal surface explorer, J. Magn. Reson. A 122 (1996) 104.
[5] S. Sharma, F. Casanova, W. Wache, A. Segre, B. Blümich, Analysis of historical porous building materials by the NMR-MOUSE(r), Magn. Reson. Imaging 21 (2003) 249.
[6] A. Guthausen, G. Zimmer, P. Blümler, B. Blümich, Analysis of polymer materials by surface NMR via the MOUSE, J. Magn. Reson. 130 (1998) 1.
[7] L.J. Schreiner, J.C. MacTavish, L. Miljkovic, M.M. Pintar, R. Blinc, G. Lahajnar, D.D. Lasic, L.W. Reeves, NMR line shape—spin–lattice relaxation correlation study of portland cement hydration, J. Am. Ceram. Soc. 68 (1985) 10.
[8] J. Greener, H. Peemoeller, C. Choi, R. Holly, E.J. Reardon, C.M. Hansson, M.M. Pintar, Monitoring of hydration of white cement paste with proton NMR spin–spin relaxation, J. Am. Ceram. Soc. 83 (2000) 623.
[9] D.D. Lasic, J.M. Corbett, J. Jian, J.C. MacTavish, M.M. Pintar, R. Blinc, G. Lahajnar, NMR spin grouping in hydrating cement at 200 MHz, Cement Concrete Res. 18 (1988) 649.
[10] A.J. Bohris, U. Goerke, P.J. McDonald, M. Mulheron, B. Newling, B.L. Page, A broad line NMR and MRI study of water and water transport in Portland cement pastes, Magn. Reson. Imaging 16 (1998) 455.
[11] J. Link, J. Kaufmann, K. Schenker, Water transport in concrete, Magn. Reson. Imaging 12 (1994) 203.
[12] J.J. Young, P. Szomolanyi, T.W. Bremner, B.J. Balcom, Magnetic resonance imaging of crack formation in hydrated cement paste materials, Cement Concrete Res. 34 (2004) 1459.
[13] E. Fukushima, J.A. Jackson, Unilateral Magnet having a Remote Uniform Field Region for Nuclear Magnetic Resonance, US Pat 6,489,872 (1999).
[14] P.T. Callaghan, G. Hunter, R. Dykstra, C.D. Eccles, NMR apparatus, New Zealand Pat, 520114 (2004).
[15] A.E. Marble, I.V. Mastikhin, B.G. Colpitts, B.J. Balcom, An analytical methodology for magnetic field control in unilateral NMR, J. Magn. Reson. 174 (2005) 78.
[16] P.M. Glover, P.S. Aptaker, J.R. Bowler, E. Ciampi, P.J. McDonald, A novel high-gradient permanent magnet for the profiling of planar films and coatings, J. Magn. Reson. 139 (1999) 90.
[17] P.J. Doughty, P.J. McDonald, Drying of coatings and other applications with GARField, in: S. Siegfried, S. Han (Eds.), NMR Imaging in Chemical Engineering, Wiley-VCH, Weinham, 2005, pp. 89–106.
[18] J.P. Gorce, D. Bovey, P.J. McDonald, P. Palasz, D. Taylor, J.L. Keddie, Vertical water distribution during the drying of polymer films from aqueous emulsions, Eur. Phys. J. E 8 (2002) 421.
[19] G. Bennett, J.P. Gorce, J.L. Keddie, P.J. McDonald, H. Berglind, Magnetic resonance profiling studies of the drying of film-forming

aqueous dispersions and glue layers, Magn. Reson. Imaging 21 (2003) 235.
[20] P.J. McDonald, A. Akhmerov, L.J. Backhouse, S. Pitts, Magnetic resonance profiling of human skin *in vivo* using GARField magnets, J. Pharm. Sci. 94 (2005) 1850.
[21] L. Backhouse, M. Dias, J.P. Gorce, J. Hadgraft, P.J. McDonald, J.W. Wiechers, GARField magnetic resonance profiling of the ingress of model skin-care product ingredients into human skin *in vitro*, J. Pharm. Sci. 93 (2004) 2274.
[22] J.D. Edwards, B.V. Jayawant, W.R.C. Dawson, D.T. Wright, Permanent-magnet linear eddy-current brake with a non-magnetic reaction plate, IEE Proc. Elect. Power Appl. 146 (1999) 627.
[23] P.J. McDonald, J. Mitchell, M. Mulheron, P.S. Aptaker, J.-P. Korb, L. Monteilhet, Two-dimensional relaxometry studies of cement pastes performed using a new one-sided NMR magnet, Cement Concrete Res. (2006), doi:10.1016/j.cemconres.2006.01.013.
[24] Y.-Q. Song, L. Venkataramanan, M.D. Hürlimann, M. Flaum, P. Frulla, C. Straley, T_1–T_2 correlation spectra obtained using a fast two-dimensional Laplace inversion, J. Magn. Reson. 154 (2002) 261.
[25] J.R. Zimmerman, W.E. Brittin, NMR studies in multiple phase systems: lifetime of a water molecule in an adsorbing phase on silica gel, J. Phys. Chem. 61 (1957) 1328.
[26] K.R. Brownstein, C.E. Tarr, Importance of classical diffusion in NMR studies of water in biological cells, Phys. Rev. A 19 (1979) 2446.
[27] P.J. McDonald, J.-P. Korb, J. Mitchell, L. Monteilhet, Surface relaxation and chemical exchange in hydrating cement pastes: a two-dimensional NMR relaxation study, Phys. Rev. E 72 (2005) 011409.
[28] K. Halbach, Physical and optical properties of rare earth cobalt magnets, Nucl. Instrum. Methods 187 (1981) 109.
[29] P.J. McDonald, Stray field magnetic resonance imaging, Prog. Nucl. Magn. Reson. Spect. 30 (1997) 69.
[30] J.-P. Korb, M. Whaley-Hodges, R.G. Bryant, Translational diffusion of liquids at surfaces of microporous materials: theoretical analysis of field-cycling magnetic relaxation measurements, Phys. Rev. E 56 (1997) 1934.
[31] J.-P. Korb, M. Whaley-Hodges, T. Gobron, R.G. Bryant, Anomalous surface diffusion of water compared to aprotic liquids in nanopores, Phys. Rev. E 60 (1999) 3097.
[32] F. Barberon, J.-P. Korb, D. Petit, V. Morin, E. Bermejo, Probing the surface area of a cement-based material by nuclear magnetic relaxation dispersion, Phys. Rev. Lett. 90 (2003) 116103.
[33] L. Monteilhet, J.-P. Korb, J. Mitchell, P.J. McDonald, Observation of exchange of micro-pore water in cement pastes by 2-dimensional T_2-T_2 nuclear magnetic resonance relaxometry, Phys. Rev. E (accepted for publication).